



NANOCRYSTALLIZATION OF AMORPHOUS Fe₃₃Zr₆₇ ALLOY

N.X. Sun, K. Zhang, X.H. Zhang, X.D. Liu*, and K. Lu*

National Key Laboratory for RSA, * also with International Centre for Materials Physics,
Institute of Metal Research, Academia Sinica, Shenyang 110015, P. R. China

(Accepted April 1996)

Abstract -- A nanocrystalline (NC) fcc FeZr₂ intermetallic compound was formed by completely crystallizing the melt-spun amorphous Fe₃₃Zr₆₇ alloy ribbons. The nanocrystallization kinetics and microstructures of the crystallized products were characterized by means of differential scanning calorimetry (DSC), X-ray diffraction (XRD), transmission electron microscopy (TEM) and optical microscopy. The NC fcc FeZr₂ samples were formed with grain sizes ranging from 11 to 24 nm, of which the microstrains were found to be extremely small ($\langle \epsilon^2 \rangle^{0.5} \leq 0.05\%$). The lattice parameters of the NC fcc FeZr₂ were measured in different grain sized samples. Avrami exponents and activation energies of the nanocrystallization process were determined, indicating the transformation began with a 2-D surface crystallization process at the free side of the ribbon followed by 3-D grain growth.

1. INTRODUCTION

In the past few years, several methods have been developed for synthesizing nanocrystalline (NC) materials, such as the inert gas condensation and the subsequent *in situ* consolidation of ultrafine powders (UFP consolidation) (1,2), ball-milling (3), electrodepositing (4), and the complete crystallization method from amorphous solids (5). Among the above routes, the complete crystallization method possesses some unique advantages, *i.e.* (i) this method is very simple, easily controlled, and can produce NC materials in a large quantity; nanocrystallization can be realized through conventional annealing in most alloy and elemental systems which can be formed in the amorphous state; (ii) because no artificial consolidation is involved in the synthesis procedures, the nm-crystallites and the interfaces are formed naturally during the nanocrystallization process; the obtained NC sample is dense with clean interfaces (6); and (iii) the presence of plenty of interfaces in the crystallized products often affects the nanocrystallization kinetics and thermodynamics significantly (7,8), so the nanocrystallization process itself provides a unique opportunity to study the interface formation process from the amorphous state. Up to now, the complete crystallization method has been successfully applied in various alloy systems to obtain NC composites, such as Ni-P (5), FeSi-B (9), Fe-Mo-Si-B (10), and to obtain single-phase NC materials, such as Co-Zr (11), Ni-Zr (12), and so on.

Formation kinetics of the NC composites through the complete crystallization method have been intensively studied (7,9), but investigations on the formation kinetics of single-phase NC materials are rare. In this paper, we report on the synthesis and characterization of an fcc FeZr₂ nanophase synthesized through the complete crystallization method. The microstrains of the crystallized NC FeZr₂ samples were quantitatively determined and compared with NC samples synthesized by means of other methods. A detailed study on the nanocrystallization kinetics of the amorphous Fe₃₃Zr₆₇ alloy ribbons was also carried out.

2. EXPERIMENTAL

Ingots of the alloy Fe₃₃Zr₆₇ (at.%) with a mass of 20-30 g were prepared by arc-melting appropriate amounts of pure metals of Fe (99.99%) and Zr (99.99%) under a high purity argon atmosphere. The ingots were then melted and quenched onto a rotating copper wheel with a tangential speed of 30 m/s. The obtained ribbons were typically 1-2 mm wide and 20-25 μm thick.

X-ray diffraction (XRD) was carried out on a Rigaku diffractometer (D/max-2400) using the CuKα radiation ($\lambda = 0.1541$ nm, reflection geometry). Transmission electron microscopy (TEM) was performed on a Philips EM420 electron microscope with an accelerating voltage of 100 kV, and the samples were thinned by Ar-ion-beam milling. Partially crystallized and as-quenched Fe₃₃Zr₆₇ alloy ribbons were etched with a FeCl₃ solution for metallographic observations.

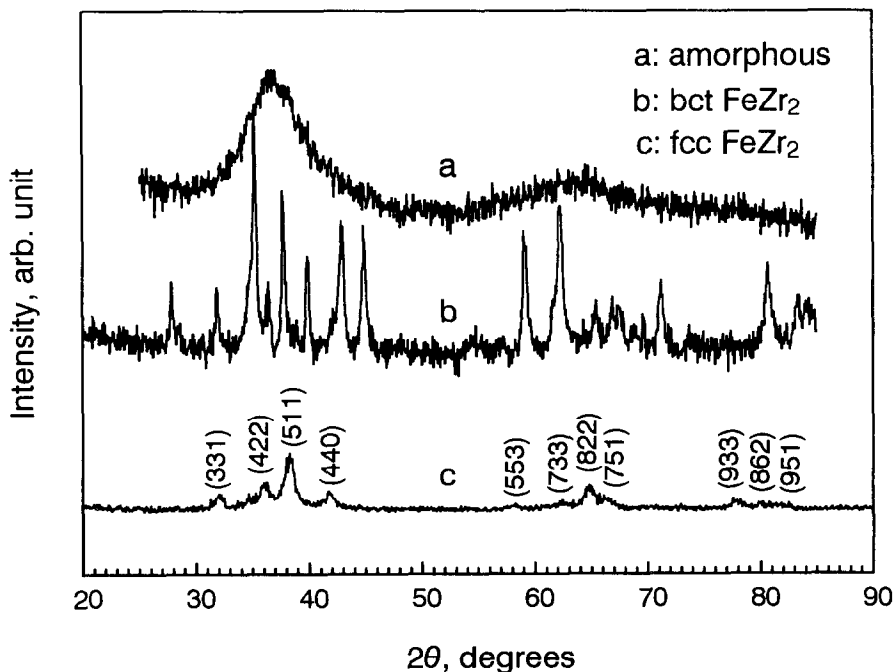


Figure 1. XRD patterns of Fe₃₃Zr₆₇ alloy ribbons, (a): as-quenched; (b): as-cast; (c): fully crystallized.

Thermal analyses were performed on a differential scanning calorimeter (DSC), PerkinElmer DSC-7, under a flowing high purity argon atmosphere. The temperature and energy of DSC were calibrated using pure Zn and In with the accuracy of ± 0.2 K for temperature and ± 0.02 mW for energy measurements. Al_2O_3 sample pans were used and the samples were around 5 mg each.

3. RESULTS AND DISCUSSION

3.1 Formation and Characterization of the fcc FeZr_2 Nanophase

The amorphism of the as-quenched $\text{Fe}_{33}\text{Zr}_{67}$ alloy ribbons was examined by both XRD and TEM. The XRD pattern of the as-quenched $\text{Fe}_{33}\text{Zr}_{67}$ alloy ribbons is shown in Figure 1(a). There are two halos in the XRD trace, exhibiting the typical characteristics of a Fe-Zr amorphous phase. The TEM micrograph of the as-quenched ribbons is shown in Figure 2(a). It is clear that the as-quenched ribbon is fully amorphous, with no crystallites visible.

Synthesis procedures of the fcc FeZr_2 nanophase were as follows: rapidly heating the as-quenched $\text{Fe}_{33}\text{Zr}_{67}$ alloy ribbons, which were enclosed in a vacuum silica tube in order to avoid oxidation, to a predetermined annealing temperature, holding at the annealing temperature for a certain period before cooling it down to room temperature. The time and temperature of the annealing process was determined from DSC isotherms, to assure that the amorphous ribbons were completely crystallized. Figure 2(b) shows a typical TEM dark-field image of the fully crystallized $\text{Fe}_{33}\text{Zr}_{67}$ alloy ribbons, showing clusters of grains in similar orientations, and the average grain size was estimated to be about 10 nm. Figures 1(b) and 1(c) show the XRD patterns of the as-cast and a fully crystallized $\text{Fe}_{33}\text{Zr}_{67}$ alloys, respectively. The as-cast $\text{Fe}_{33}\text{Zr}_{67}$ alloy contains a stable

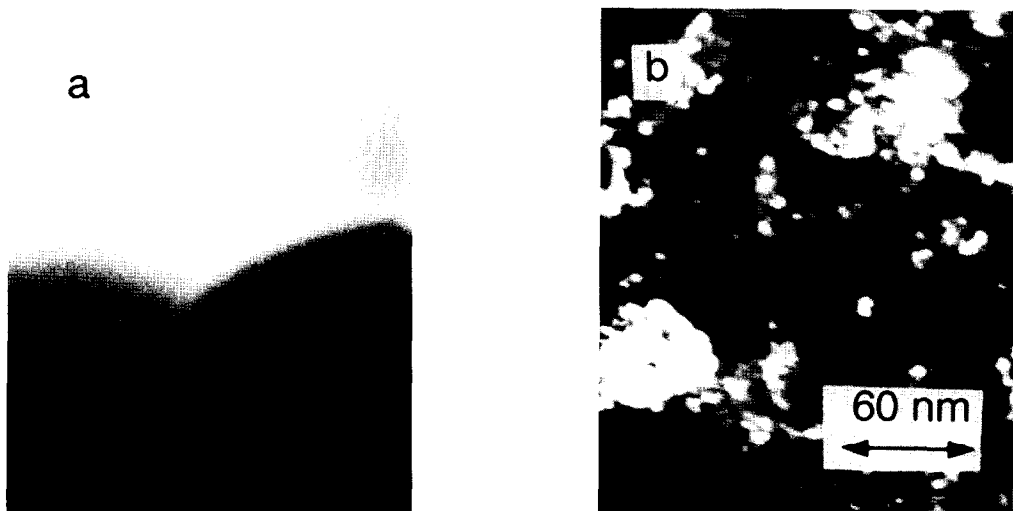


Figure 2. (a) Bright field image of the as-quenched $\text{Fe}_{33}\text{Zr}_{67}$ alloy ribbons, (b) dark field TEM micrograph of a fully crystallized fcc FeZr_2 sample.

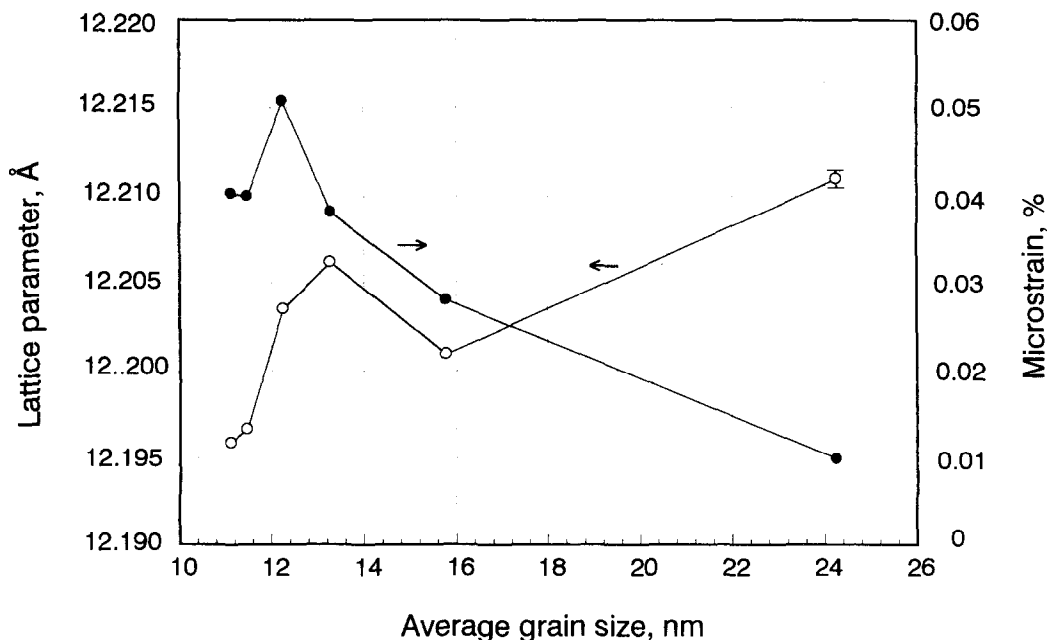


Figure 3. Room temperature values of lattice parameter (open circles), and microstrain (closed circles) of fcc FeZr₂ nanocrystalline material with different average grain sizes.

bct FeZr₂ phase, while the fully crystallized product is the fcc FeZr₂ nanophase, with a NiTi₂ structure (13). It is clear that the diffraction lines of the fcc FeZr₂ nanophase are considerably broadened due to the refinement of the crystallites and/or an increase in the microstrain.

Quantitative XRD experiments were carried out in order to determine the average grain size and the microstrain in the fcc FeZr₂ nanophase. By assuming Cauchy size and Cauchy strain, we get the following equation to separate the two broadening effects:

$$B = 0.89 \lambda / (d \cos \theta) + 4 \operatorname{tg} \theta \langle \varepsilon^2 \rangle^{0.5} \quad [1]$$

where B is the full width at half maximum (FWHM) of the Bragg peak at θ , the first term is the crystal size broadening, and the second one is the strain broadening, d is the grain size and the term $\langle \varepsilon^2 \rangle^{0.5}$ is the rms (root-mean-square) strain. Accordingly, the average grain sizes d and the microstrains of the NC fcc FeZr₂ samples were determined from the X-ray diffraction lines of (331), (440), (553), (771) and (12 2 2) after a correction for $K\alpha$ and instrumental broadening. The lattice parameter a of the fcc FeZr₂ nanophase was determined through an extrapolation of $\cos^2 \theta (1/\sin \theta + 1/\theta)$ from these diffraction lines listed above.

TABLE 1
Heat Treatment Conditions and the Resultant Average Grain Sizes for the Crystallized fcc FeZr₂ Nanophase from an Amorphous Fe₃₃Zr₆₇ Alloy

Sample No.	A	B	C	D	E	F
Temperature, °C	390	370	410	365	360	490
Time, min	30	60	25	100	155	30
Grain size, nm	11	11	12	13	16	24

TABLE 2
Comparison of the Typical Microstrain Values in NC Materials Prepared by Different Methods

NC alloys	<i>d</i> , nm	$\langle \epsilon^2 \rangle^{0.5}$, %	Synthesis method, reference
Pd	20	0.21	gas-condensation, (14)
Pd	76	0.26	severe plastic deformation, (14)
Pd	86	0.36	ball-milling, (14)
fcc FeZr ₂	12	0.05	complete crystallization, this work
fcc FeZr ₂	24	0.01	complete crystallization, this work

Note that the average grain sizes *d* and microstrains $\langle \epsilon^2 \rangle^{0.5}$ of NC-Pd were determined from a single X-ray diffraction peak by a fitting of Voigt functions.

The average grain sizes of the NC fcc FeZr₂ samples obtained from various heat treatment processes are shown in Table 1, ranging from 11 nm to 24 nm. The lattice parameters and the microstrains with different average grain sizes of the NC fcc FeZr₂ samples are shown in Figure 3.

The lattice parameters of the obtained NC FeZr₂ samples range from $a = 12.1959 \pm 0.0005$ Å at $d = 11$ nm to $a = 12.2109 \pm 0.0005$ Å at $d = 24$ nm; all are higher than 12.177 nm, the literature a value for fcc FeZr₂ phase in reference (13). The microstrain values in the NC fcc FeZr₂ samples are in the range of 0.01% to 0.05%, which are extremely small compared with the detected microstrain values in NC materials synthesized by means of other methods. Table 2 shows a comparison of the microstrains in several samples prepared by means of different synthesis methods: the complete crystallization method, the gas-condensation method, the ball-milling method, and the severe plastic deformation method. The microstrains of the crystallized NC fcc FeZr₂ samples are $\langle \epsilon^2 \rangle^{0.5} = 0.01\%$ when $d = 24$ nm, and $\langle \epsilon^2 \rangle^{0.5} = 0.05\%$ when $d = 12$ nm; while microstrains of the NC Pd samples (average grain sizes *d* all exceed 20 nm) prepared by the gas-condensation method, the severe plastic deformation method and the ball-milling method are

0.21%, 0.26% and 0.36%, respectively (14). Other microstrain values detected in various NC materials synthesized by the gas-condensation method and the ball-milling method are in the range of 0.25% to 1.0% when $d < 30$ nm (15-17). It is clear that the microstrains in the fcc FeZr₂ nanophases prepared by the complete crystallization method are an order of magnitude lower than those in NC Pd synthesized by the gas-condensation method, the severe deformation method and the ball-milling method. Direct HRTEM observation of the UFP consolidated NC Pd revealed that a high density of defect structures, including dislocations, twins, nanovoids and localized disordered regions existed in grain boundaries and triple junctions. No nanovoids or localized disordered regions were observed in NC Ti₇₀Ni₂₀Si₁₀ and (Fe_{0.99}Mo_{0.01})₇₈Si₉B₁₃ alloys, which were synthesized through the complete crystallization method (18). This implies that the strains in NC materials prepared through the gas-condensation method are much higher than those in NC materials crystallized from amorphous solids.

This phenomenon evidently can be understood according to their synthesis procedures. In the UFP consolidation method, ultrafine powders are often consolidated at a pressure of 1-5 GPa in order to obtain bulk nanostructured materials with a high density (1). In the ball-milling method and the severe plastic deformation method, precursors are subjected to severe deformation prior to the formation of NC materials. In contrast, in the complete crystallization method, NC material is obtained through an annealing of the amorphous precursor at a temperature of about $T_m / 2$ of the corresponding crystalline phase (19), so the NC materials are formed naturally, no artificial consolidation or deformation is involved. Furthermore, much of the microstrain in the crystallized nanophase can be eliminated at such an annealing temperature. So, it is conceivable that the microstrains in NC materials synthesized through the gas-condensation method, the ball-milling method and the severe deformation method are much higher than those in the NC materials prepared by the complete crystallization method. Therefore, we may conclude that the complete crystallization method can provide us with NC materials not only with dense and clean interfaces, but also with much less microstrain than in NC materials synthesized by the gas condensation method, the ball-milling method and the severe deformation method.

3.2 Nanocrystallization Kinetics of the Amorphous Fe₃₃Zr₆₇ Alloy Ribbons

3.2.1 Activation energy

According to the peak shifts of the linear heating DSC curves at different heating rates, the apparent activation energy of crystallization can be obtained by using the Kissinger technique (20). The Kissinger equation is as follows:

$$\ln(B / T^2) = -E / RT + \text{Constant} \quad [2]$$

where B is the heating rate, E the apparent activation energy for the process, R the gas constant and T a specific temperature such as peak temperature T_p or onset temperature T_{on} , which can be measured at selected heating rates B . By plotting $\ln(B / T^2)$ versus $1 / (RT)$, a straight line with a slope of E will be obtained, where E is the apparent activation energy of the whole reaction. The heating rates of the dynamic DSC scans were chosen as 80, 40, 20, 10 and 5 K/min. The Kissinger plots, $\ln(B / T^2)$ versus $1 / (RT)$, are shown in Figure 4. The obtained activation energies for the crystallization process of the as-quenched Fe₃₃Zr₆₇ alloy ribbons were 271 ± 2 kJ/mol for T_{on} and 272 ± 2 kJ/mol for T_p , respectively.

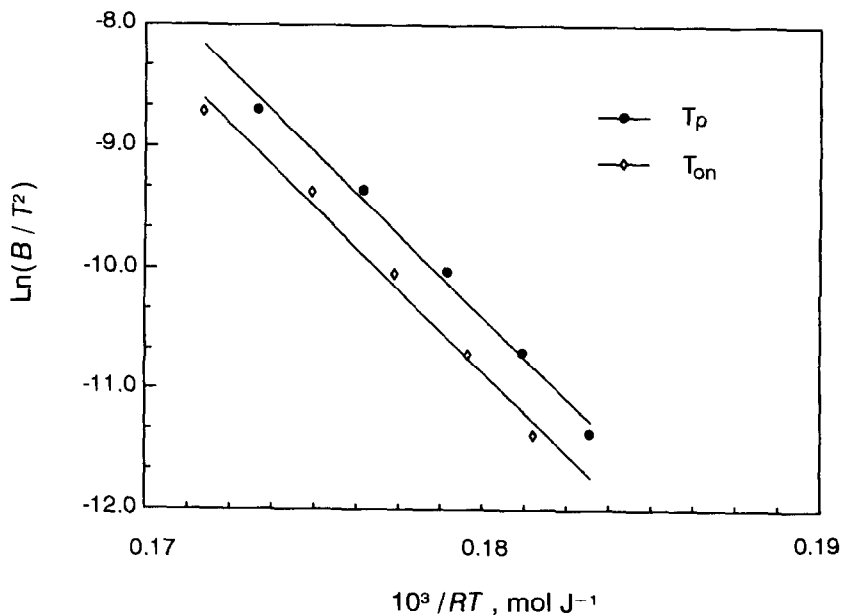


Figure 4. Kissinger plots of $\ln(B/T^2)$ versus $1/(RT)$ obtained from linear heating DSC scans.

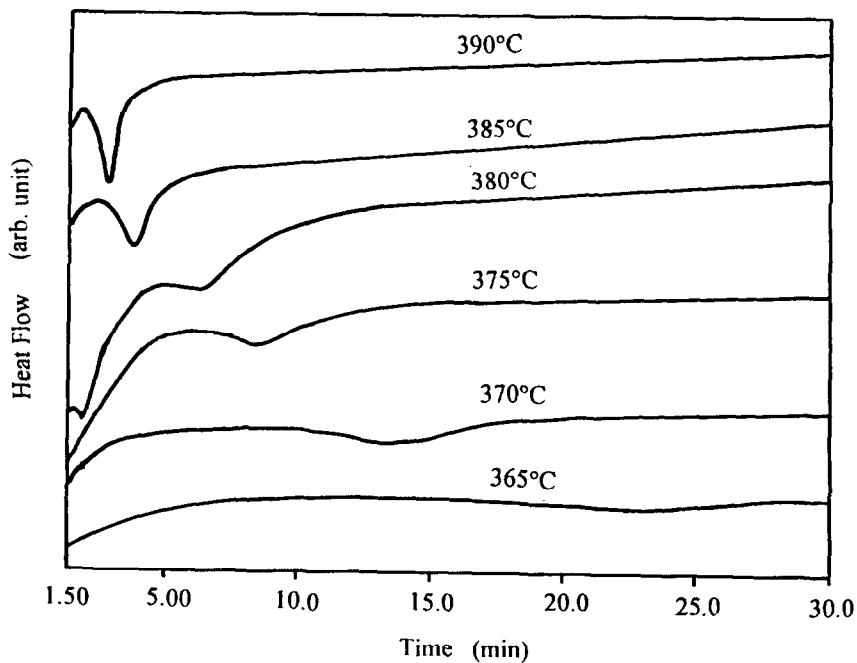


Figure 5. Isothermal DSC curves of different annealing temperatures.

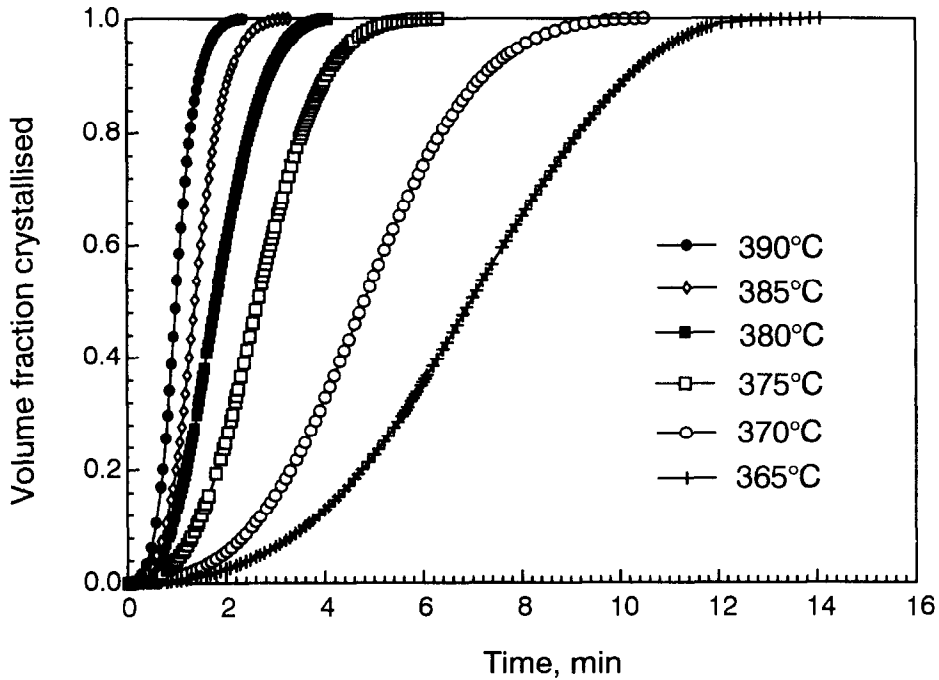


Figure 6. Plots of $x(t)$ vs. t obtained from isothermal DSC scans.

Isothermal annealing of the as-quenched $\text{Fe}_{33}\text{Zr}_{67}$ alloy ribbons was performed in the DSC at six annealing temperatures: 390, 385, 380, 375, 370 and 365°C. The isothermal DSC curves are shown in Figure 5; each of them exhibits a single exothermal peak, implying a polymorphous crystallization process. By integrating the isothermal DSC curves up to different time t , the volume fractions crystallized, $x(t)$, at different temperatures were obtained as shown in Figure 6.

The activation energy can also be evaluated from the data of isothermal crystallization processes. This was done by applying an Arrhenius type relation to the time required for a fixed amount of transformation at different temperatures, i.e.

$$t(x) = t_0 \exp(E_c(x) / RT) \quad [3]$$

where $t(x)$ is the time required to transform volume fraction x , t_0 a time constant and $E_c(x)$ the activation energy. The plot of $\ln t(x)$ versus $1 / (RT)$ will give a straight line with a slope of $E_c(x)$. The obtained activation energies for the crystallization process of the as-quenched $\text{Fe}_{33}\text{Zr}_{67}$ alloy ribbons are shown in Figure 7, exhibiting an average activation energy of 290 ± 5 kJ/mol when $x < 90\%$.

Spassov and Köster (21) have derived the grain growth activation energy for nanocrystalline FeZr_2 to be 290 ± 23 kJ/mol, which coincides well with the present activation energies obtained by the Arrhenius method, 290 ± 5 kJ/mol, but is a little higher than 272 ± 2 kJ/mol, the apparent activation energy obtained from the Kissinger method. Buschow (13) has derived the activation

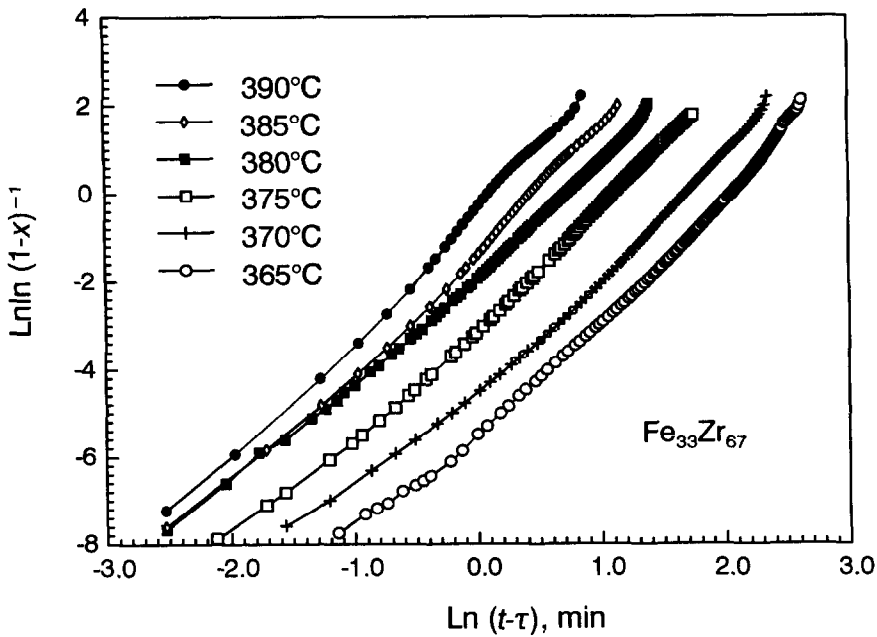


Figure 7. Activation energy $E_d(x)$ versus x obtained from isothermal DSC scans.

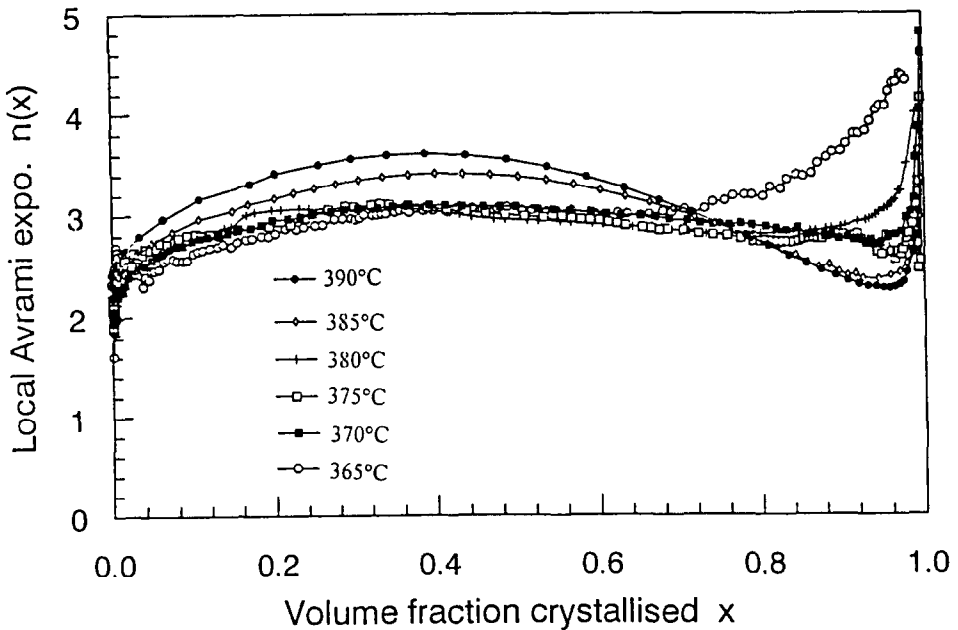


Figure 8. Avrami plots of $\ln \ln (1-x)^{-1}$ versus $\ln (t - \tau)$ at different temperatures obtained from isothermal DSC scans.

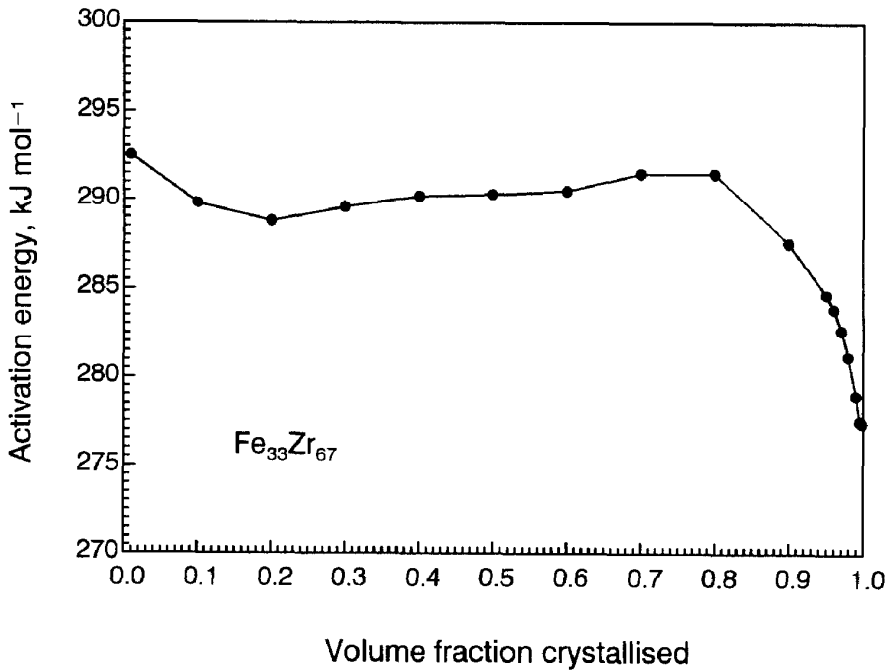


Figure 9. Local Avrami exponents $n(x)$ versus x , obtained from isothermal crystallization process.

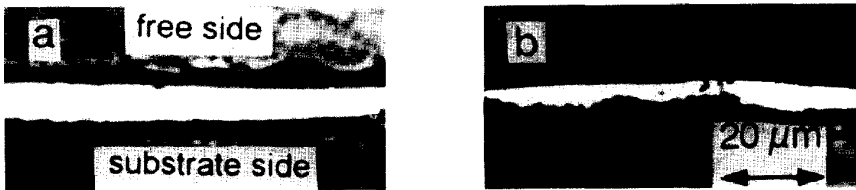


Figure 10. Metallographs of the $Fe_{33}Zr_{67}$ alloy ribbons: (a) as-quenched; (b) partially crystallized.

energy for the crystallization of amorphous $Fe_{33}Zr_{67}$ alloys using the Kissinger method to be 368 kJ/mol, which is much higher than all the activation energies listed above. The reason for this discrepancy may be as follows. If linear grain growth is assumed, the apparent activation energy Q for polymorphic crystallization can be written as (22):

$$Q = [E_n + (n - 1) E_g] / n \quad (l > 0) \quad [4]$$

$$Q = E_g \quad (l = 0) \quad [5]$$

where, E_n is the activation energy for nucleation, E_g the activation energy for grain growth, n the Avrami exponent, and I the nucleation rate. So, if the crystallization process of the amorphous Fe₃₃Zr₆₇ alloy ribbons is dominated by grain growth, *i.e.* the nucleation rate $I = 0$, then $Q = E_g$, just as what we have obtained; however, if nucleation is involved, just as what is often expected in a polymorphic crystallization process of amorphous alloys, then $Q = [E_n + (n - 1) E_g] / n$, which will be higher than E_g , just as what has been obtained in reference (13). Accordingly, the nanocrystallization process of the present amorphous Fe₃₃Zr₆₇ alloy ribbons is grain growth dominated.

3.2.2 Local Avrami Exponent, $n(x)$

Quantitative description of the isothermal crystallization kinetics of amorphous solids is often made by means of the Kolmogorov-Johnson-Mehl-Avrami (KJMA) equation (23):

$$x(t) = 1 - \exp[- K (t - \tau)^n] \quad [6]$$

where $x(t)$ is the volume fraction transformed at time t , τ is the incubation time or time lag, and n is the Avrami exponent which reflects the nucleation rate and/or the growth morphology. K is the pre-exponential factor, a kinetic parameter depending on the annealing temperature, nucleation rate and growth rate. For isothermal crystallization, the Avrami plot of $\ln \ln(1-x)^{-1}$ versus $\ln(t - \tau)$ should give a straight line with a slope of n . Figure 8 shows the Avrami plots of $\ln \ln(1-x)^{-1}$ versus $\ln(t - \tau)$. Clearly, the Avrami plots are not linear, which implies that the local Avrami exponents (defined as $n(x) = \partial \ln \ln(1-x)^{-1} / \partial \ln(t - \tau)$ (24)) are not constant during the whole crystallization process, but are as shown in Figure 9.

The calculated local Avrami exponents $n(x)$ for the crystallization process of the present as-quenched Fe₃₃Zr₆₇ alloy ribbons are about 2.0 at the beginning of the nanocrystallization process, which implies that the nanocrystallization process began with a two dimensional (2-D) grain growth or a constant one dimensional (1-D) nucleation and subsequent grain growth process according to the classical KJMA equation. In order to determine the actual process between the above two possibilities, metallographs of the cross-section of the as-quenched and the partially crystallized Fe₃₃Zr₆₇ alloy ribbons are shown in Figure 10; it is obvious that the nanocrystallization process began from the free side of the ribbon. Because there exists the possibility of a higher density of quenched-in nuclei in the free side than in the substrate side due to the different cooling rates in the two sides of the ribbon (25), so the nanocrystallization process of the present Fe₃₃Zr₆₇ alloy ribbons began with a 2-D grain growth dominated surface crystallization process at the free side.

With the increase of x , the dimensionality of grain growth changes from 2 into 3, so the local Avrami exponents increase to $n = 3.0$ at about $x = 30\%$. When $x < 70\%$, the local Avrami exponents of the 365°C, 370°C, 375°C and 380°C isothermal crystallization processes are about 3.0, implying that the nanocrystallization processes were 3-D grain growth dominated at these temperatures according to the classical KJMA equation, which is consistent with the result obtained by the apparent activation energies. The local Avrami exponents of the 385°C, 390°C crystallization processes all exceed 3.0, implying that nucleation was also involved in high temperature crystallization process. When $x > 95\%$, the local Avrami exponents, $n(x)$, all rise sharply to about 4.0. The anomalous rise of the local Avrami exponents at high x has also been

observed in the crystallization processes of various metallic glasses (26,27), and a detailed analysis will be given elsewhere.

It is interesting to note that the local Avrami exponent, $n(x)$, of the nanocrystallization process of the amorphous Fe₃₃Zr₆₇ alloy rises monotonously when $x > 95\%$; while the apparent activation energy, $E_c(x)$, drops monotonously from about 290 kJ/mol when $x = 90\%$, to 277 kJ/mol at $x = 99\%$. There must exist some correlation between $n(x)$ and $E_c(x)$, and further investigation is still needed.

4. CONCLUSIONS

1. NC fcc FeZr₂ samples with the average grain sizes ranging from 11 nm to 24 nm have been synthesized by a complete crystallization of amorphous Fe₃₃Zr₆₇ alloy ribbons.

2. The measured lattice parameters of the fcc FeZr₂ nanophases were in the range of 12.1959 ± 0.0005 to 12.2109 ± 0.0005 Å, and the detected microstrain values in them were extremely small ($\langle \epsilon^2 \rangle^{0.5} \leq 0.05\%$), compared with those measured in NC materials synthesized through the gas-condensation method, the ball-milling method and the severe plastic deformation method.

3. Investigations on the nanocrystallization kinetics of the amorphous Fe₃₃Zr₆₇ alloy ribbons showed that the nanocrystallization process began with a 2-D surface crystallization process at the free side of the ribbon, followed by a 3-D grain growth.

ACKNOWLEDGMENT

The authors want to thank Prof. U. Köster for helpful suggestions. Financial support from the National Natural Science Foundation of China, the Chinese Academy of Sciences and the Liaoning Provincial Completed Doctoral Foundation are acknowledged.

REFERENCES

1. H. Gleiter, *Prog. Mater. Sci.* **33**, 223 (1989).
2. R.W. Siegel, in *Physics of New Materials*, ed. F.E. Fujita, Springer Series in Materials Science, Vol. 27, Springer-Verlag, Berlin, p. 65 (1994).
3. C.C. Koch, *Nanostruct. Mater.* **2**, 109 (1993).
4. U. Erb, A.M. El-Sherik, G. Palumbo, and K.T. Aust, *Nanostruct. Mater.* **2**, 383 (1993).
5. K. Lu, J.T. Wang, and W.D. Wei, *J. Appl. Phys.* **69**, 522 (1991); *Scripta Metall. Mater.* **24**, 2319 (1990).
6. M.L. Sui, K. Lu, W. Deng, L.Y. Xiong, S. Patu, and Y.Z. He, *Phys. Rev. B* **44**, 6466 (1991); *J. Appl. Phys.* **69**, 4451 (1991).
7. R. Lück, K. Lu and W. Frantz, *Scripta Metall. Mater.* **28**, 1071 (1993).
8. K. Lu, R. Lück and B. Predel, *J. Alloy Comp.* (1995), in print.
9. H.Y. Tong, J.T. Wang, B.Z. Ding, K. Lu, *J. Non-cryst. Solids* **150**, 444 (1992).
10. X.D. Liu, J.T. Wang and B.Z. Ding, *Scripta Metall. Mater.* **28**, 59 (1993).
11. M.M. Nicolaus, H.-R. Sinning, and F. Haessner, *Mat. Sci. Eng.* **A150**, 101 (1992).
12. C. Beeli, H.-U. Nissen, Q. Jiang and R. Lück, *Mat. Sci. Eng.* **A133**, 346 (1991).
13. K.H.J. Buschow, *J. Less-Common Metals* **79**, 243 (1981).
14. H.-E. Schaefer, R. Würschum, T. Gessmann, G. Stöckl, P. Scharwächter, W. Frank, R.Z. Valiev, H.-J. Fecht, and C. Moelle, *Nanostruct. Mater.* **6**, 869 (1995).

15. J.A. Eastman, M.A. Beno, G.S. Knapp and L.J. Thompson, *Nanostruct. Mater.* **6**, 543 (1995).
16. H.-J. Fecht, *Nanostruct. Mater.* **6**, 33 (1995).
17. A. Teresiak, H. Kubsch, *Nanostruct. Mater.* **6**, 671 (1995).
18. D.H. Ping, Ph.D. thesis, Institute of Metal Research Academia Sinica, (1995).
19. K. Lu, *Acta Metall. Mater. Sinica* **30**, B1 (1994) in Chinese.
20. H.E. Kissinger, *Anal. Chem.* **29**, 1702 (1957).
21. T. Spassov and U. Köster, *J. Mater. Sci.* **28**, 2789 (1993).
22. S. Ranganathan, *J. Mater. Sci.* **16**, 2401 (1981).
23. J.W. Christian, *The Theory of Transformations in Metals and Alloys*, 2nd ed. Pergamon Press, Oxford (1975).
24. A. Calka and A.P. Radlinski, *MRS Symp. Proc.* **80**, 203 (1987).
25. A.S. Schaafsma, H. Snijders, F. van der Woude, J.W. Drijver and S. Radelaar, *Phys. Rev. B.* **20**, 4423 (1979).
26. G. Ghosh, M. Chandrasekaran and L. Delaey, *Acta Metall. Mater.* **39**, 925 (1991).
27. K. Lu, X.D. Liu and F.H. Yuan, submitted to *Physica B*.